J Supercond Nov Magn (2015) 28:1649–1658
DOI 10.1007/s10948-015-3019-4

LETTER

Magnetocaloric Properties of $La_{0.85}Ag_{0.15}MnO_3$ and $(La_{0.80}Pr_{0.20})_{0.85}Ag_{0.15}MnO_3$ Compounds

Ali Osman Ayaş · Mustafa Akyol · Selda Kılıç Çetin · Gönül Akça · Ahmet Ekicibil · Bekir Özçelik

Received: 9 December 2014 / Accepted: 10 February 2015 / Published online: 24 February 2015

Abstract In this work, the structural and magnetic properties of the polycrystalline $La_{0.85}Ag_{0.15}MnO_3$ (LAM) and $(La_{0.80}Pr_{0.20})_{0.85}Ag_{0.15}MnO_3$(LPAM) compounds prepared by the sol–gel method were investigated. The structural properties of both polycrystalline compounds were investigated by X-ray diffraction (XRD), scanning electron microscope (SEM), and energy dispersive X-ray spectrum (EDX) methods. The XRD results showed that both samples crystallized in the hexagonal symmetry with $R\bar{3}c$ space group. The SEM images showed that the particles are closely packed with each other, and their size range from 0.5 to 2.0 μm with the average sizes of 1.23 and 1.03 μm, for LAM and LPAM, respectively. From the EDX spectrum, in both compounds, we did not see loss of any integrated elements during the sintering process and no other impurity elements. The magnetic properties were studied by employing temperature $M(T)$ and external magnetic field $M(H)$ dependence of magnetization measurements. Both compounds showed magnetic phase transition from paramagnetic to ferromagnetic phase. With the substitution of Pr for La, the Curie temperature, T_C, decreased from 262 to 216 K. At a field change of 5 T, LAM and LPAM showed large magnetic entropy changes of 7.90 and 4.96 J kg^{-1} K^{-1}, respectively. Furthermore, their relative cooling power (RCP) values were found as 213.32 and 263.02 J kg^{-1}, respectively. These findings make both LAM and LPAM compounds as good candidates for the practical magnetic refrigeration.

Keywords Magnetic materials · Magnetic properties · Sol–gel method

1 Introduction

Magnetocaloric effect (MCE) yields a unique way of obtaining the refrigeration in a large temperature interval including ultra-low and room temperatures. By increasing the magnetic field, magnetic entropies decrease and a heat is radiated from the magnetic system into the environment through an isothermal process. On the contrary, by decreasing the magnetic field, magnetic entropies increase and a heat is absorbed from the lattice system into the magnetic system through an adiabatic process [1].

Due to the promising environment-friendly and the energy efficient magnetic cooling systems, comparing with the well-known gas-compression refrigeration, the room temperature magnetic cooling based on MCE has attracted attention in recent years [2]. MCE has been studied in a large variety of magnetic materials [3]. Among these, perovskite manganites which are formed in $RE_{1-x}A_xMnO_3$ (RE: rare earth cation, A: alkali metal, or alkaline earth cation) have proven to be beneficial for potential applications because of their interesting properties, such as convenient preparation, exhibiting high chemical stability, higher resistivity (which lowers Eddy current losses), much smaller thermal and field hysteresis than any rare earth and 3d-transition metal-based alloys, and cheapest material among existing magnetic refrigerants [4, 10]. Furthermore, the Curie temperatures and saturation magnetizations of the

A. O. Ayaş (✉)
Department of Physics, Faculty of Sciences and Letters, Adıyaman University, 02040 Adıyaman, Turkey
e-mail: aayas@adiyaman.edu.tr

M. Akyol · S. K. Çetin · G. Akça · A. Ekicibil · B. Özçelik
Department of Physics, Faculty of Sciences and Letters, Çukurova University, 01330 Adana, Turkey

perovskite manganite materials can be adjusted by varying their compositions [6, 8, 9]. Among manganites, the $La_{1-x}Ag_xMnO_3$ ($0.0 \leq x \leq 1.0$) series are one of the most famous materials because of having Curie temperature values around room temperature and exhibiting large MCE comparable to that of Gd-based alloys [11]. These manganites are also well-known materials exhibiting the transition from paramagnetic phase to ferromagnetic one like others. The nature of this transition has been explained on the basis of Zener's double-exchange theory [12]. Further investigations have confirmed that several parameters, which induced by changing average A-site ionic radius value, such as bond length of Mn–O, bond angle of Mn–O–Mn, and ionic size mismatch, strongly affect the physical and magnetic properties of these systems [13, 15]. In order to have a better understanding of these parameters, in this study, the effect of reduction of the mean ionic radius of the A site was investigated. Additionally, although there are a lot of research works about $La_{1-x}Ag_xMnO_3$ series in the literature, there is no work related to Pr substitution into this matrix. We have, therefore, selected Ag-based $La_{0.85}Ag_{0.15}MnO_3$(LAM) and some amount of Pr substitution for La, in order to obtain $(La_{0.80}Pr_{0.20})_{0.85}Ag_{0.15}MnO_3$(LPAM) compound. Then, we have explored the magnetocaloric properties of those compounds for the purpose of finding new kind of magnetocaloric materials to evaluate their refrigeration efficiency with applicability at various temperature intervals. As a result, we have reported the magnetocaloric properties of LAM with and without the effect of doping totally 0.17 Pr^{3+} into the A site.

2 Experimental Procedure

Polycrystalline samples of $La_{0.85}Ag_{0.15}MnO_3$ (LAM) and $(La_{0.80}Pr_{0.20})_{0.85}Ag_{0.15}MnO_3$(LPAM) were prepared via sol–gel method by using high purity powders of La_2O_3, $Mn(NO_3)_2 \cdot 4H_2O$ and $AgNO_3$for LAM and La_2O_3, $Pr(NO_3)_3 \cdot 6H_2O$, $Mn(NO_3)_2 \cdot 4H_2O$, and $AgNO_3$ for LPAM as starting materials. Hydrochloric acid with 37 % purity, monoethylene glycol with 99.9 % purity, citric acid monohydrate with 99.9 % purity, and nitric acid with 70 % purity, ≥99.999 % trace metals basis were used as a chelating substance. Obtained materials were mixed and heated by magnetic stirrer at 300 °C until obtaining gel-like precipitation. The precipitation was heated at 500 °C for 1 h to burn and then calcined at 550 °C for 5 h. The final materials were grounded by using an agate mortar to obtain fine powder. After that, the microcrystalline powder was pressed to make disc-shaped samples and finally, these disc-shaped samples were sintered at 970 °C for 24 h in air. The crystal structure of the powder sample was determined by X-ray diffraction (XRD) method using Cu Kα radiation (Rigaku RadB-DMAX II), and the analyses of the samples carried out by Match! 2 program which based on Rietveld refinement method. The crystallite sizes, D, were calculated by using the Debye–Scherrer formula

$$D = \frac{k\lambda}{\beta \cos\theta} \tag{1}$$

where k is the crystallite factor (it was considered as 0.94), λ is the X-ray wavelength (Cu K_α = 1,5406 Å), and β is the peak full width at half maxima (in radians) at the observed peak angel θ. The grain structure was observed with a scanning electron microscope (SEM), and the compositional properties were investigated by energy-dispersive X-ray spectroscopy (EDX) (Zeiss EVO-40). The temperature and magnetic field dependences of the magnetization, $M(T)$ and $M(H)$, were investigated by using a Quantum Design Physical Properties Measurement System (PPMS). The magnetic entropy changes ΔS_M were obtained from the isothermal magnetization curves.

3 Results and Discussions

The XRD patterns of the samples are exhibited in Fig. 1. The patterns are sharp and can be indexed as a rhombohedral structure with $R\bar{3}c$ space group (hexagonal setting). However, a weak reflection was observed related to the presence of Ag_3O (ICDD number 01-074-0878) phase at $2\theta = 38.42°$. The unit cell parameters obtained on the basis of crystallographic data and crystallite sizes were calculated by using the Debye–Scherrer formula are tabulated in Table 1. From Table 1, it is clear that the unit cell volume and parameters decrease with the substitution of the Pr La site. The reason of this small decreasing in unit cell parameters might be linked mismatch of ionic radius of Pr^{3+} and La^{3+} [3, 11, 16]. Due to the reduction of the ionic radius of the A site might also affect Mn–O–Mn bond angle, which may result in a random distribution of magnetic exchange interaction. In addition, this may cause a large rotation of the MnO_6 octahedra [17].

In order to understand insight on the microstructure of the compounds, SEM images and EDX spectra analysis were performed for both samples. The SEM and EDX spectra results for LAM and LPAM samples are shown in Fig. 2a–b, respectively. The SEM images of samples have revealed that the samples constitute of closely packed homogeneous particles, ranging from 0.5 to 2.0 μm. The average particle sizes were found as 1.23 and 1.03 μm for LAM and LPAM taking into 100 arbitrary grains in SEM images, respectively. These values are significantly larger than the values determined from XRD spectrum by (1). This is because each grain observed by SEM basically consists of several crystallites [18]. The EDX analysis indicated

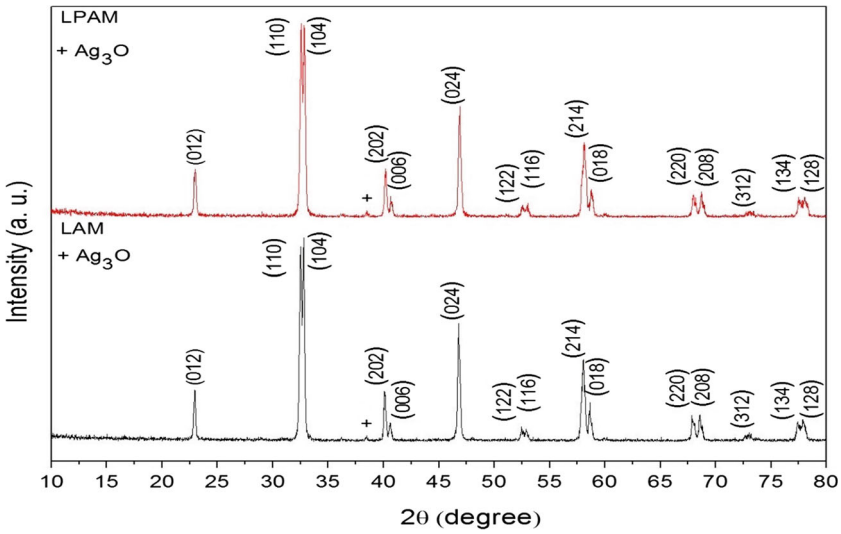

Fig. 1 XRD patterns of $La_{0.85}Ag_{0.15}MnO_3$ and $(La_{0.80}Pr_{0.20})_{0.85}Ag_{0.15}MnO_3$ samples

Table 1 Unit cell parameters and average crystallite sizes of $La_{0.85}Ag_{0.15}MnO_3$ and $(La_{0.80}Pr_{0.20})_{0.85}Ag_{0.15}MnO_3$ samples

Sample	*a* (Å)	*b* (Å)	*c* (Å)	*V* (Å^3)	*D* (nm)
$La_{0.85}Ag_{0.15}MnO_3$	5.522	5.522	13.373	353.24	19.05
$(La_{0.80}Pr_{0.20})_{0.85}Ag_{0.15}MnO_3$	5.511	5.511	13.298	349.81	17.43

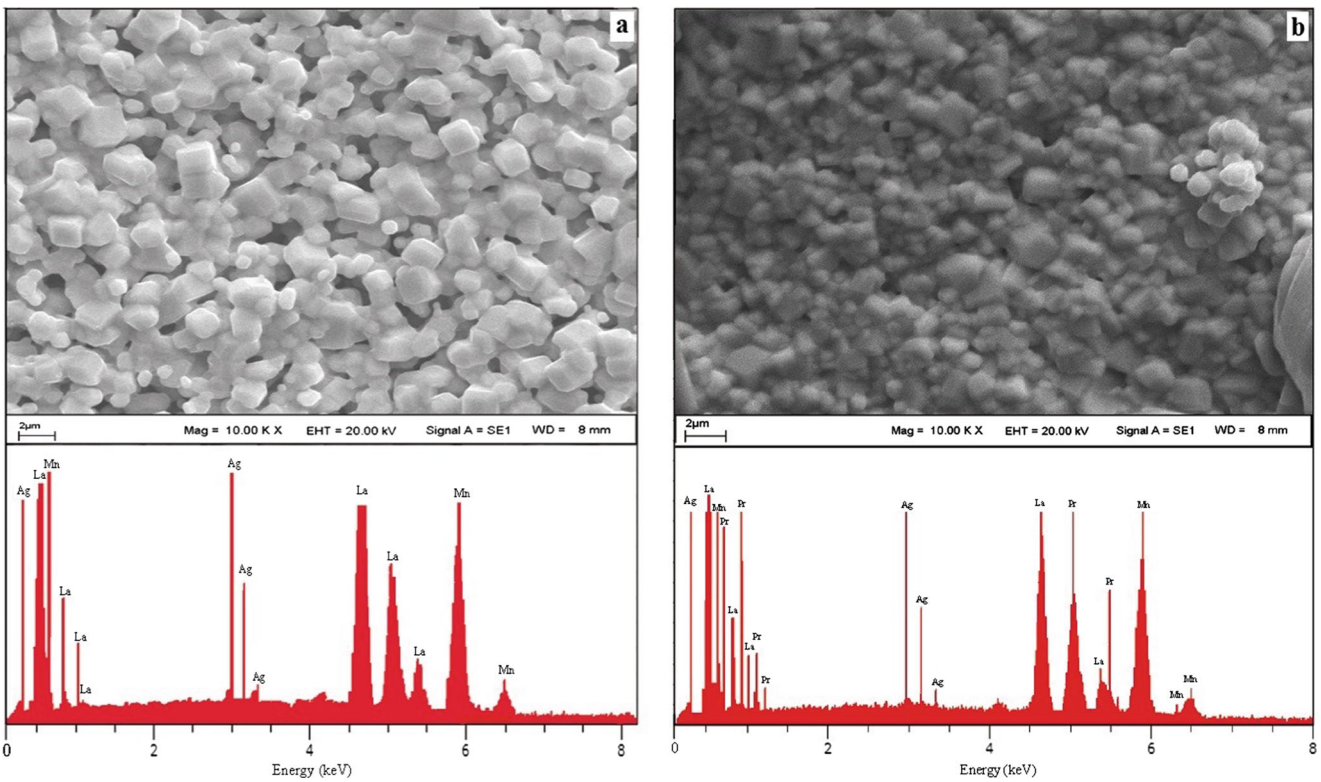

Fig. 2 SEM images and EDX spectrum of the compounds **(a)** $La_{0.85}Ag_{0.15}MnO_3$ and **(b)** $(La_{0.80}Pr_{0.20})_{0.85}Ag_{0.15}MnO_3$

Table 2 Atomic and weight percentages of La, Pr, Ag, and Mn elements in the $La_{0.85}Ag_{0.15}MnO_3$ and $(La_{0.80}Pr_{0.20})_{0.85}Ag_{0.15}MnO_3$ samples

Elements	Atomic percentage (%)		Weight percentage (%)	
	LAM	LPAM	LAM	LPAM
La	49.49		28.10	28.09
Pr	–	4.11	–	2.47
Ag	1,80	34.56	2.01	48.10
Mn	48.71	11.81	69.89	21.34

that both samples contain the expected elements (La, Pr, Ag, and Mn), which confirms that there is no loss of any integrated elements and impurities during the sintering process. Obtained amounts are given in Table 2. The analysis, except for Ag amount, showed a good homogeneity of the samples with compositions. This difference of Ag may be resulted from the limited solubility of the silver in manganites. From the exchange of some La peak in the EDX spectra of LAM with the Pr peaks in the LPAM and the similarity of those peak intensities and trace lines, it can be argued that Pr was successfully integrated into the crystal structure of LAM.

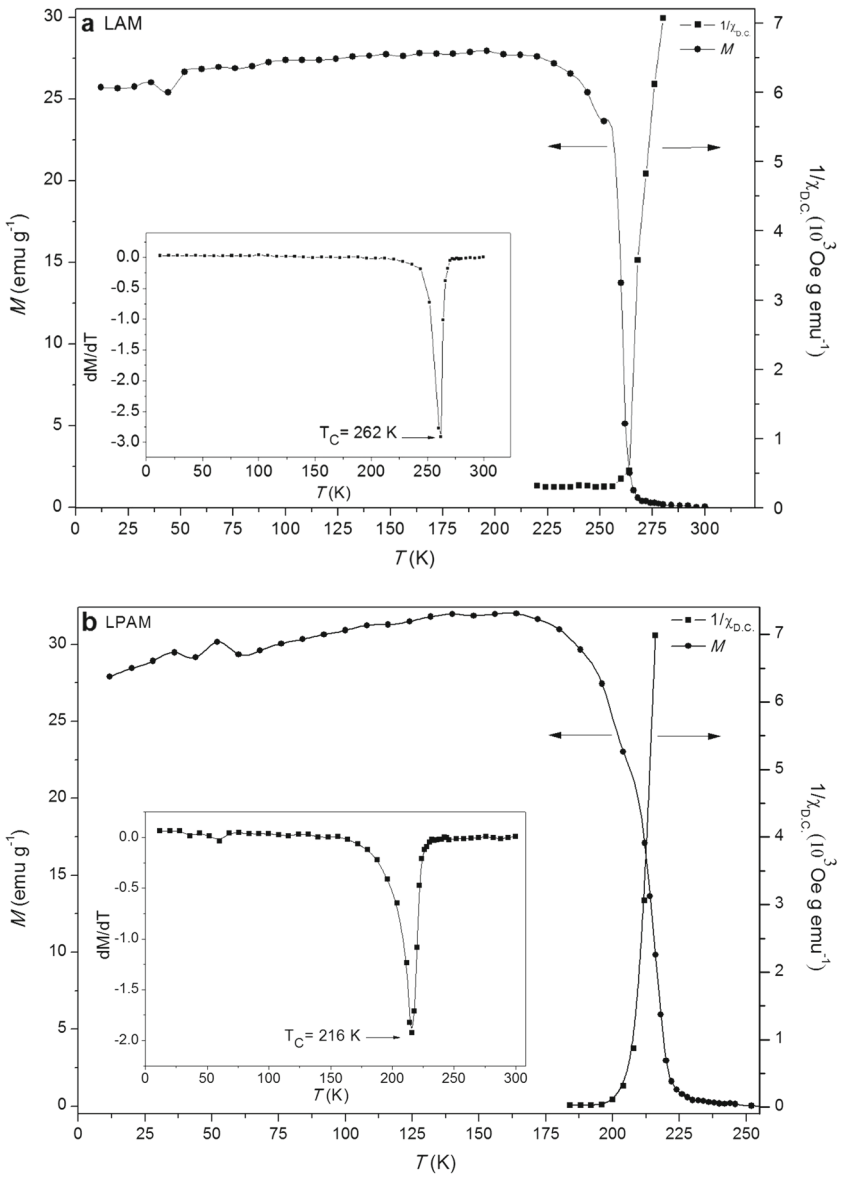

Fig. 3 $M(T)$ for the **(a)** $La_{0.85}Ag_{0.15}MnO_3$ and **(b)** $(La_{0.80}Pr_{0.20})_{0.85}Ag_{0.15}MnO_3$ samples. *Left axes*: temperature dependence of magnetization under 25 mT magnetic field. *Right axes*: the temperature dependence of the DC inverse susceptibility. *Inset*: the temperature dependence of *dM/dT*

Table 3 The maximum magnetic entropy changes and the corresponding Curie temperature for Ag-based samples

Sample	T_C(K)	$-\Delta S_M$(J kg^{-1} K^{-1})	ΔH(T)	Reference
$La_{0.95}Ag_{0.05}MnO_3$	214	1.10	1	11
$La_{0.80}Ag_{0.20}MnO_3$	300	2.40	1	19
$La_{0.75}Ag_{0.25}MnO_3$	306	1.52	1	11
$La_{0.70}Ag_{0.30}MnO_3$	306	1.35	1	11
$La_{0.85}Ag_{0.15}MnO_3$	262	2.49	1	Present work
$(La_{0.80}Pr_{0.20})_{0.85}Ag_{0.15}MnO_3$	216	1.81	1	Present work

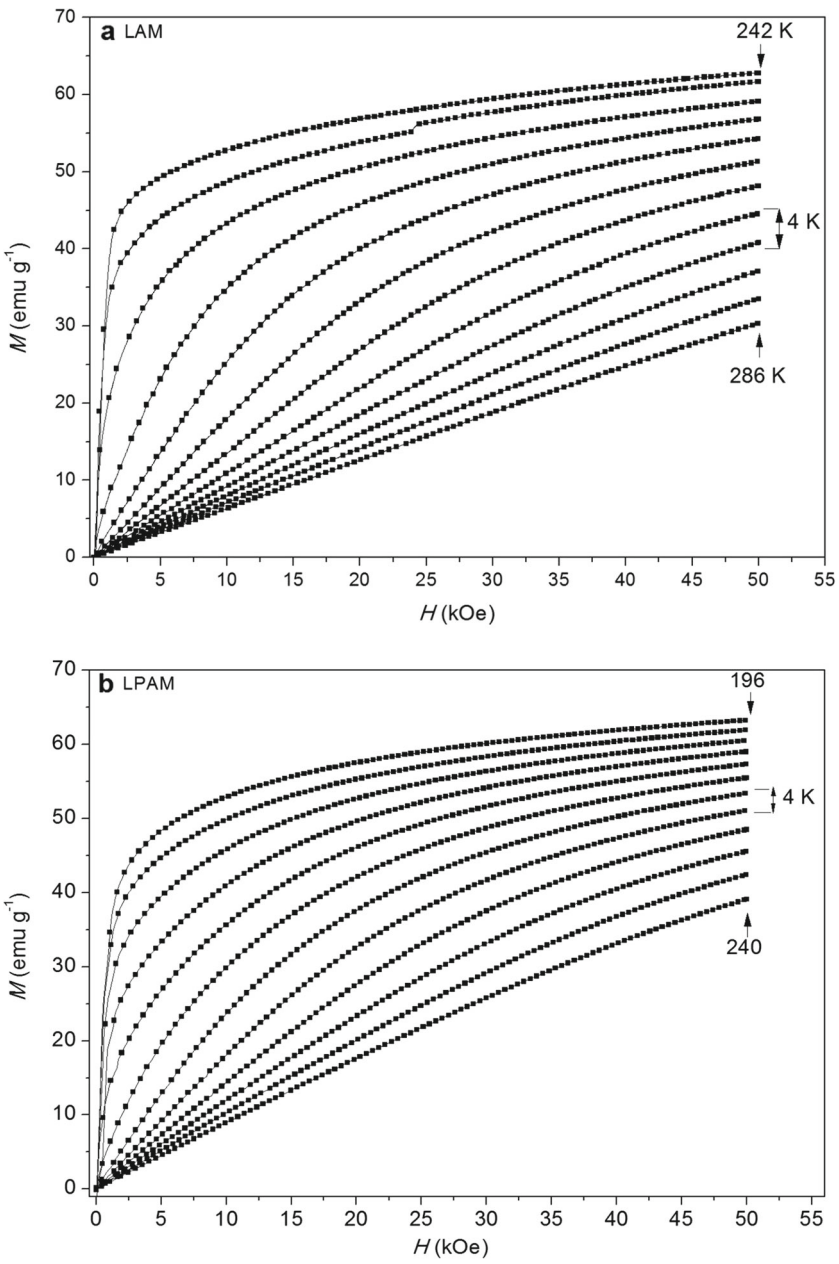

Fig. 4 Magnetic field dependences of the magnetization at the temperatures from 242 to 286 K and 196 to 240 K ($\Delta T = 4$ K) for the **a** $La_{0.85}Ag_{0.15}MnO_3$ and **b** $(La_{0.80}Pr_{0.20})_{0.85}Ag_{0.15}MnO_3$ samples, respectively

Table 4 $-\Delta S_M$(J kg^{-1} K^{-1}) and RCP values of $La_{0.85}Ag_{0.15}MnO_3$ and $(La_{0.80}Pr_{0.20})_{0.85}Ag_{0.15}MnO_3$ samples

Applied magnetic field (T)	LAM		LPAM	
	$-\Delta S_M$(J kg^{-1} K^{-1})	RCP (J kg^{-1})	$-\Delta S_M$(J kg^{-1} K^{-1})	RCP (J kg^{-1})
1	2.49	32.28	1.81	32.66
2	4.40	79.17	3.01	81.08
3	6.20	124.07	3.80	117.97
4	7.43	178.29	4.40	193.38
5	7.90	213.32	4.96	263.02

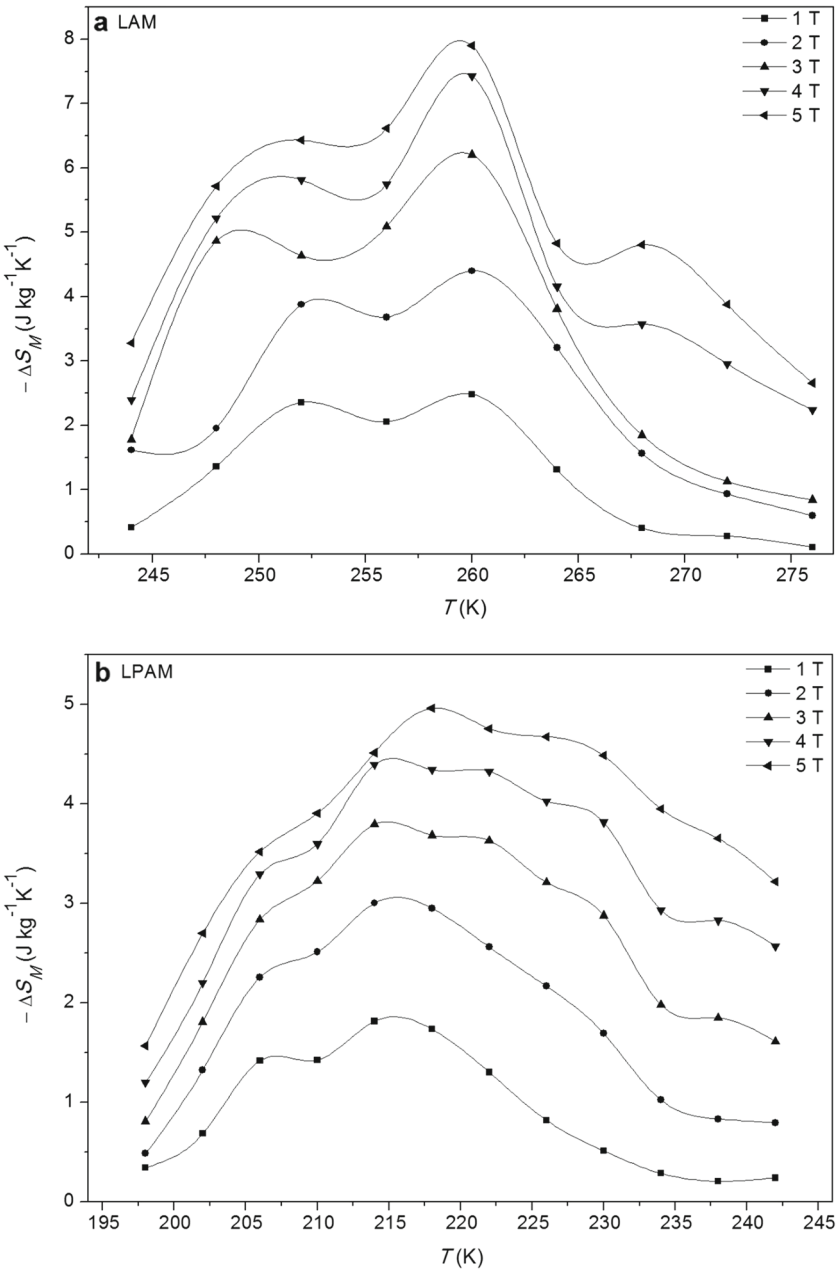

Fig. 5 The temperature dependence of ΔS_M for the **a** $La_{0.85}Ag_{0.15}MnO_3$ and **b** $(La_{0.80}Pr_{0.20})_{0.85}Ag_{0.15}MnO_3$ samples under 1, 2, 3, 4, and 5 T applied magnetic fields

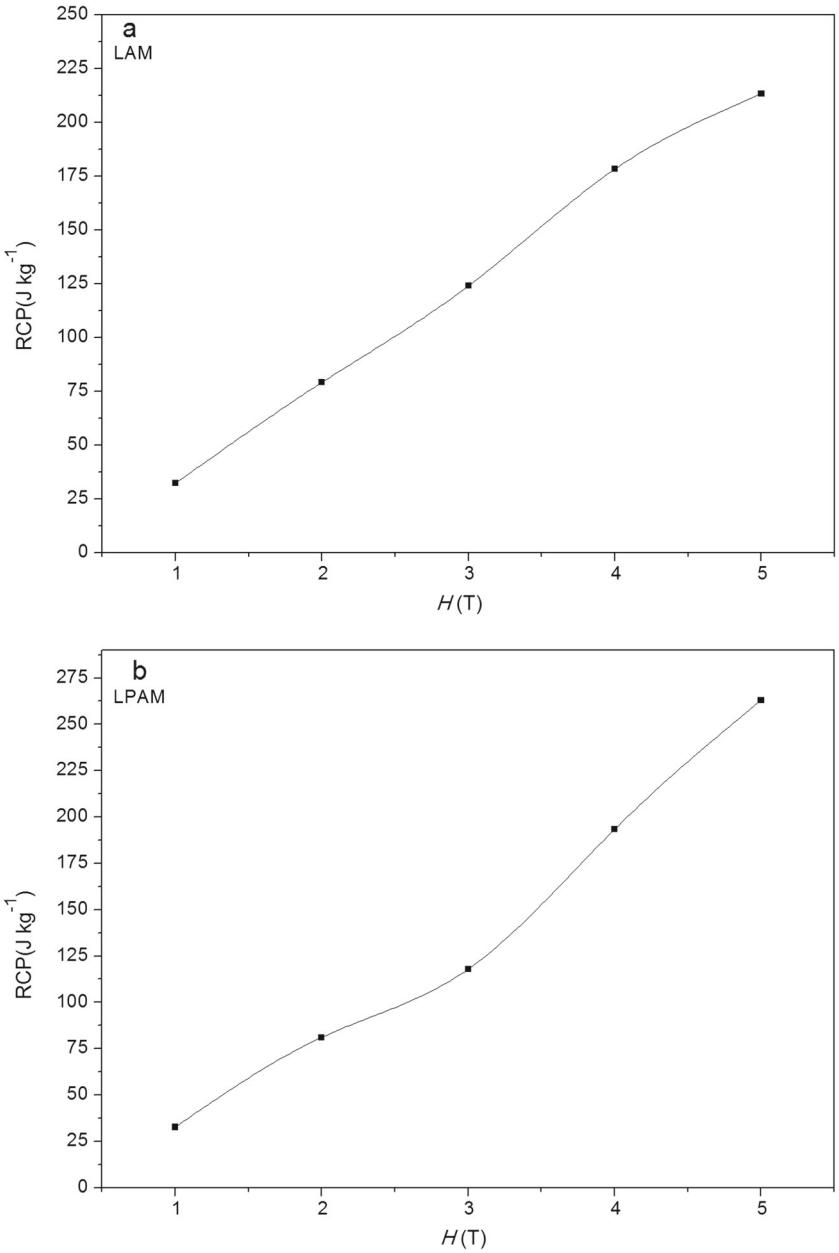

Fig. 6 The applied magnetic field dependence of RCP for the **a** $La_{0.85}Ag_{0.15}MnO_3$ and **b** $(La_{0.80}Pr_{0.20})_{0.85}Ag_{0.15}MnO_3$ samples under 1, 2, 3, 4, and 5 T magnetic fields

Figure 3a–b shows temperature dependence of magnetization $M(T)$ curves under 25 mT magnetic field (zero-field-cooling (ZFC) condition was applied for both LAM and LPAM samples). It is clearly seen from Fig. 3a–b that both samples exhibit a single magnetic phase transition at the Curie temperature, T_C. The samples behave ferromagnetically at low temperatures below T_C and paramagnetically above T_C as shown in Fig. 3a–b. The transition temperatures deduced from the minimum of dM/dT versus T curves, and some literature findings are listed in Table 3 for comparison. As can be seen from Table 3, T_C reduces from 262 to 216 K by the substitution of Pr for La in LAM. The reduction in T_C can be explained in terms of decreasing the average A-site cation size $< r_A >$ [11, 17]. The Mn–O bond length and Mn–O–Mn bond angle also decrease due to this reduction. This also strongly affects the movement of electrons between Mn^{3+} and Mn^{4+} ions. Additionally, the reduction of mean ionic radius of the A site increases the mismatch effect [17, 19]. As a result, strongly affected electron movements and increased mismatch effect weaken the double-exchange interaction; therefore the reason of decreasing at $T_C$can be attributed to this weakening effect [19]. Plots of the inverse susceptibility, $1/\chi$, versus T are also shown in the right axes of Fig. 3a–b. The figures show reasonably linear behaviors with temperature above T_C and can be fitted to the Curie–Weiss law given by $\chi = C/(T - \theta)$, where C is the Curie constant and θ is the paramagnetic Curie temperature. The Curie constant is

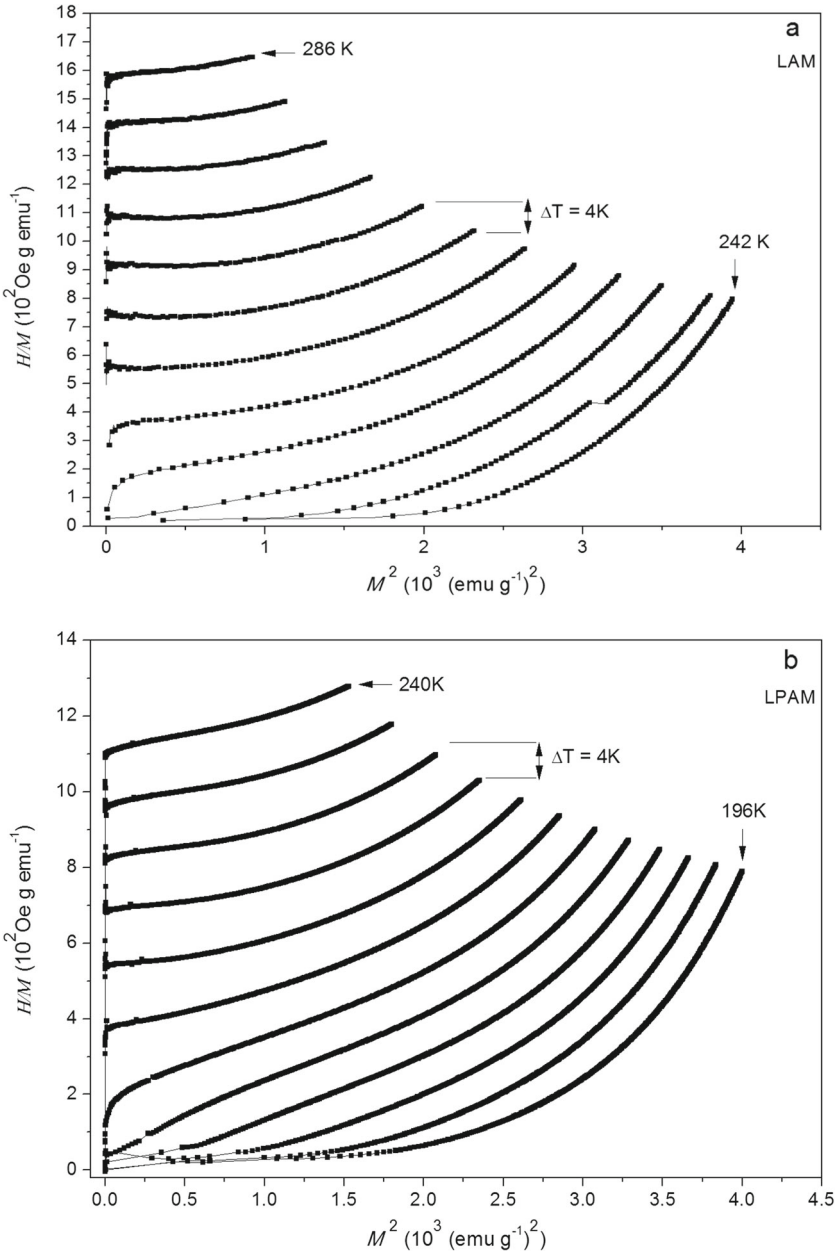

Fig. 7 H/M vs. M^2 plots around T_C for the **a** $La_{0.85}Ag_{0.15}MnO_3$ and **b** $(La_{0.80}Pr_{0.20})_{0.85}Ag_{0.15}MnO_3$ samples

given by $C = \frac{N\mu_{\text{eff}}^2\mu_B^2}{3k_B}$, where N is the Avogadro's number, mu_B is the Bohr magneton, k_B is the Boltzmann constant, and μ_{eff} is the effective magnetic moment which determined as 4.17 and 4.07 μ_B for LAM and LPAM, respectively. The effective magnetic moment value decreases by the substituting of Pr with La. This decreasing supports the picture of a canted spin arrangement in the LPAM.

Figure 4a–b shows the isothermal magnetization curves for both samples. These M–H curves were obtained at temperatures intervals of 4 K both below and above the Curie temperatures of the samples with respect to the external applied magnetic fields up to 5 T. Based on the thermodynamic theory, the magnetic entropy change, (ΔS_M), resulting from the spin ordering and inducing by the variation of the applied magnetic field from 0 to H_{max}, can be derived from the thermodynamic Maxwell relation [20],

$$\left(\frac{\partial S}{\partial H}\right)_T = \left(\frac{\partial M}{\partial T}\right)_H \tag{2}$$

through integrating over the magnetic field H,

$$\Delta S_M(T,H) = \int_0^{H}{}_{\max}\left(\frac{\partial M}{\partial T}\right) dH \tag{3}$$

where H_{max} is the final applied magnetic field. According to (3), the magnetic entropy variation, ΔS_M, depends on the temperature gradient of the magnetization and attains

a maximum value around T_C at which the magnetization decays most rapidly. For magnetization measured at discrete field and temperature intervals, the magnitude of the magnetic entropy variation defined in (3) can be approximated as [21];

$$|\Delta S_M(T, H)| = \sum_i \frac{M_i - M_{i+1}}{T_{i+1} - T_i} \Delta H \quad (4)$$

where M_i and M_{i+1} are the magnetization values taken at temperatures T_i and T_{i+1}, respectively. For both samples, the magnetic entropy changes, $\Delta S_M(T)$, versus temperature for different applied magnetic fields are presented in Table 4 and exhibited in Fig. 5a–b. The maximum of the magnetic entropy changes observed for LAM and LPAM was found to be 7.90 and 4.96 J kg^{-1} K^{-1} at 5 T applied magnetic field, respectively.

From the cooling perspective, it is important to consider not only the magnitude of the magnetic entropy change but also the relative cooling power (RCP), corresponding to the amount of heat transfer between the cold and the hot sinks in the ideal refrigeration cycle is defined as;

$$RCP(S) = \left|\Delta S_{M_{max}}\right| \times \delta T_{FWHM}, \quad (5)$$

where δT_{FWHM} is the full width at half maximum of the ΔS_M curve [22]. The RCP values for both samples were determined by (5), which are tabulated in Table 4 and plotted in Fig. 6a–b. Maximum RCP values under $\Delta H = 5$ T were found as 213.32 and 263.02 J kg^{-1} for LAM and LPAM, respectively. We should emphasize that the RCP value increases, while ΔS_M value decreases by substitution of Pr with La into LAM, because of expanding of temperature interval. The RCP value of LPAM is comparable with the reported values [3]. The magnetic entropy change, and the RCP values are larger than most of the reported perovskite materials [3, 11, 15, 17, 19, 23, 24]. Substitution of Pr with La into LAM reveals an increasement at the temperature intervals of magnetic entropy change curve. It is obvious that these results are high enough to make our samples potential candidates for magnetic refrigeration.

To determine the nature of the magnetic transition of the samples, Arrot plots of H/M versus M^2 covering a broad temperature range around T_C are also plotted in Fig. 7a–b. The positive slopes are clearly observed from Fig. 7a–b, indicating the occurrence of the second-order magnetic phase transition.

4 Conclusions

We have investigated the structural, magnetic, and magnetocaloric properties of polycrystalline $La_{0.85}Ag_{0.15}MnO_3$ and Pr-substituted $(La_{0.80}Pr_{0.20})_{0.85}Ag_{0.15}MnO_3$ samples produced by the sol–gel method. XRD results show that both samples are crystallized in the rhombohedral structure with $R\bar{3}c$ space group (hexagonal setting); however, a weak reflection occurs at $2\theta = 38.42°$, which can be identified as Ag_3O. Unit cell volume and lattice parameters decrease with the substitution of Pr for La. SEM observations show that the particles are closely packed and their sizes range from 0.5 to 2.0 μm with the average particle size of 1.23 and 1.03 μm for LAM and LPAM, respectively. The ferromagnetic to paramagnetic phase transitions were observed at $T_C \sim 262$ and 216 K for LAM and LPAM, respectively. T_C reduces via Pr substitution for La, and the Arrot plots reveal the second-order nature of magnetic transitions for both samples. We have also found large magnetic entropy changes for both samples, given as 7.90 and 4.96 J kg^{-1} K^{-1} at 5 T applied magnetic field change, respectively. Furthermore, the RCP values at a field change of $H = 5$ T are 213.32 and 263.02 J kg^{-1} for LAM and LPAM, respectively. All these results indicate that the LAM and LPAM can be considered as good candidates for magnetic refrigeration. Additionally, our results are interesting enough to pave the way for investigations of materials useful for magnetic refrigeration.

Acknowledgments The Research Fund of Çukurova University, Adana, Turkey, supported this work under grant contract numbers FEF2013BAP16 and FEF2010D11. The authors thank also Dr. Deniz Takcıfor his technical assistance in XRD measurements and Mr. Deniz Çetin for language assistance.

References

1. Shen, B.G., Suon, J.R., Hu, F.X., Zhang, H.W., Cheng, Z.H.: Adv. Mater. **21**, 4545–4564 (2009)
2. Pecharsky, V.K., Gschneidner Jr., K.A.: J. Appl. Phys. **86**, 565 (1999)
3. Phan, M.H., Yu, S.C.: J. Magn. Magn. Mater. **308**, 325–340 (2007)
4. Wang, Z., Xu, Q., Ni, G., Zhang, H.: Physica B **406**, 4333–4337 (2011)
5. Kolat, V.S., Izgi, T., Kaya, A.O., Bayri, N., Gencer, H., Atalay, S.: J. Magn. Magn. Mater. **322**, 427–433 (2010)
6. Phan, M.H., Tian, S.B., Hoang, D.Q., Yu, S.C., Nguyen, C., Ulyanov, A.N.: J. Magn. Magn. Mater. **258–259**, 309–311 (2003)
7. Chau, N., Nhat, H.N., Luong, N.H., Minh, D.L., Tho, N.D., Chau, N.N.: Physica B **327**, 270–278 (2003)
8. Fan, J., Pi, L., Zhang, L., Tong, W., Ling, L., Hong, B., Shi, Y., Zhang, W., Lu, D., Zhang, Y.: Physica B **406**, 2289–2292 (2011)
9. Çetin, S.K., Acet, M., Ekicibil, A., Sarıkürkçü, C., Kıymaç, K.: J. Alloys Compd. **565**, 139–143 (2013)
10. Rebello, A., Naik, V.B., Mahendiran, R.: J. Appl. Phys. **110**, 013906 (2011)
11. Tang, T., Gu, K.M., Cao, Q.Q., Wang, D.H., Wang, S.Y., Zhang, S.Y., Du, Y.W.: J. Magn. Magn. Mater. **222**, 110 (2000)

12. Zener, C.: Phys. Rev. **81**, 440 (1951)
13. Millis, A.J., Littlewood, P.B., Shraiman, B.J.: Phys. Rev. Lett. **74**, 5144 (1995)
14. Goodenough, J.B.: Phys. Rev. **100**, 5144 (1995)
15. Thaljaoui, R., Boujelben, W., Pekala, M., Pekala, K., Fagnard, J.-F., Vanderbemden, P., Donten, M., Cheikhrouhou, A.: J. Magn. Magn. Mater. **352**, 6–12 (2014)
16. Kallel, N., Kallel, S., Hagaza, A., Oumezzine, M.: Physica B **404**, 285–288 (2009)
17. M'nassri, R., Cheikhrouhou-Koubaa, W., Koubaa, M., Boudjada, N., Cheikhrouhou, A.: Solid State Commun. **151**, 1579–1582 (2011)
18. Das, S., Dey, T.K.: J. Phys. D: Appl. Phys. **40**, 1855 (2007)
19. Hien, N.T., Thuy, N.P.: Physica B. **319**, 168 (2002)
20. A.H. Morrish: The Physical Principles of Magnetism. Wiley, New York (1965). Chapt.3
21. Foldeaki, M., Chahine, R., Bose, T.K.: J. Appl. Phys. **77**, 3528 (1995)
22. Gschneidner, K.A., Pecharsky, V.K.: Annu. Rev. Mater. Sci **30**, 387 (2000)
23. Xu, Q.Y., Gu, K.M., Liang, X.L., Ni, G., Wang, Z.M., Sang, H., Du, Y.W.: J. Appl. Phys. **90**, 524 (2001)
24. Chen, W., Nie, L.Y., Zhong, W., Shi, Y.J., Hu, J.J., Li, A.J., Du, Y.W.: J. Alloys Compd. **395**, 23 (2005)